Optimizing Growth of Yttrium-Iron-Garnet Films for Spintronic Applications

MS Thesis

By

Javed Ali

August 15, 2024

Supervised By

Dr Muhammad Sabieh Anwar

LUMS

A Not-for-Profit University

DEPARTMENT OF PHYSICS,

SYED BABAR ALI SCHOOL OF SCIENCE AND ENGINEERING

LAHORE UNIVERSITY OF MANAGEMENT SCIENCES,

LAHORE, PAKISTAN.

This work is submitted as a thesis in the partial fulfillment of the requirements for the degree of Master of Science in Physics, to the Department of Physics, Lahore University of Management Sciences, Lahore, Pakistan.

Declaration of Authenticity

I, **Javed Ali**, hereby declare that this thesis is my own work and has been written independently. All sources used in the preparation of this thesis have been duly acknowledged.

_____ **Signature**

LUMS
A Not-for-Profit University

Research Completion Certificate

This is to certify that the thesis entitled *"Optimizing Growth of Yttrium Garnet films for Spintronic Applications"* submitted by Javed Ali (2022-12-0008), has been thoroughly evaluated and accepted. The scope and quality of the research presented in this work meet the standards required for the partial fulfillment of the Master of Science degree.

Supervisor

Dr. Muhammad Sabieh Anwar
Associate Professor
Department of Physics
Lahore University of Management Sciences
(LUMS), Lahore, Pakistan

Dedication

To my dearest and loving partner, whose endless love, unwavering faith, and constant support have been my greatest source of strength. Your encouragement has made this journey not only possible but truly meaningful. This work is a reflection of our shared dreams and the incredible bond we share. Thank you for being my everything.

Acknowledgement

I owe my deepest gratitude and heartfelt thanks to my advisor, Dr. Muhammad Sabieh Anwar, whose invaluable guidance and unwavering support have been instrumental throughout my research. His boundless enthusiasm and passion for science have been a constant source of inspiration, driving me to explore new avenues and gain deeper insights. Dr. Sabieh Anwar has instilled in me a rigorous scientific approach and the importance of clear and precise presentation of research. It has been an immense honor to work and study under his supervision.

I also wish to extend my sincere appreciation to my co-advisor, Dr. Syed Adnan Raza. His steadfast optimism and thoughtful concern have been crucial to the completion of this study. Dr. Adnan has imparted a wealth of knowledge with kindness and patience. His guidance and encouragement have made him an exceptional source of learning and inspiration for me. I am deeply grateful for all he has taught me and for his enduring support. Finally, I am eternally thankful to my family. To my mother, whose boundless love, unwavering prayers, and countless sacrifices have been the foundation of all my achievements—your support has been my guiding light. Without your relentless belief in me, this work would not have been possible.

To my brother, Abid Ali, whose financial and emotional support, encouragement, and sacrifices have been invaluable throughout my studies—your unwavering support has given me the strength to persevere. I am deeply grateful for your constant presence and the countless ways you have helped me reach this milestone.

<div align="right">

Javed Ali

August 15, 2024

</div>

Abstract

Yttrium Iron Garnet ($Y_3Fe_5O_{12}$, YIG) is a ferrimagnetic insulator with a remarkably low Gilbert damping constant (α), making it an ideal candidate for spintronics and magnonics applications. This thesis presents a detailed investigation into the magnetization dynamics of nanoscale thick YIG films deposited on GGG substrates with (100) and (111) orientations. Using radio frequency (RF) magnetron sputtering and oxygen environment annealing, we systematically studied the impact of growth conditions on the Gilbert damping constant.

The structural characteristics of the films were analyzed using X-ray diffraction (XRD) technique, revealing insights into their crystal structure and surface morphology. Static magnetic properties were evaluated with magneto-optic Kerr ellipsometry (MOKE) and vibrating sample magnetometry (VSM), while magnetization dynamics were probed using vector network analyzer ferromagnetic resonance (VNA-FMR). Through a thorough exploration of film thicknesses and annealing parameters, we achieved significant reductions in the Gilbert damping constant, with the lowest recorded value being $\alpha = 2.1 \times 10^{-3}$.

This research contributes to the fundamental understanding of YIG thin films and highlights their potential for advancing spin-based technologies. The findings underscore the importance of precise control over growth parameters in enhancing the performance of magnetic materials. Furthermore, the thesis outlines future research directions, including the study of the inverse spin Hall effect (ISHE), to further explore the practical implications and potential applications of optimized magnetization dynamics in YIG films.

خلاصہ

یٹریئم آئرن گارنیٹ (Y$_3$Fe$_5$O$_{12}$, YIG) ایک فیرومقناطیسی انسولیٹر ہے جس کا ڈیمپنگ کانسٹنٹ غیر معمولی طور پر کم ہے، جو اسے سپنٹرونکس اور میگنونس کی ایپلیکیشنز کے لیے ایک مثالی امیدوار بناتا ہے۔ یہ مقالہ GGG سبسٹریٹس (100) اور (111) اور ریٹیشنز پر بنائی گئی نینو میٹر موٹی YIG فلموں کی مقناطیسی متحرکات کی تفصیلی تحقیق پیش کرتی ہے۔ ریڈیو فریکوئنسی (RF) میگنیٹرون سپٹرنگ اور آکسیجن ماحول میں اینیلنگ کا استعمال کرتے ہوئے، ہم نے بڑھوتری کی حالتوں کا گلبرٹ ڈیمپنگ کانسٹنٹ پر اثر کا منظم طریقے سے مطالعہ کیا۔

فلموں کی ساختی خصوصیات کا تجزیہ ایکس رے ڈفریکشن (XRD) تکنیک کا استعمال کرتے ہوئے کیا گیا، جو ان کی کرسٹل ساخت اور سطحی مرفالوجی کے بارے میں معلومات فراہم کرتا ہے۔ غیر متحرک مقناطیسی خصوصیات کو وائبریٹنگ سیمپل میگنیٹومیٹری (VSM) اور میگنیٹوآپٹک کر ایلپسومیٹری (MOKE) کے ذریعے جانچا گیا، جبکہ مقناطیسی متحرکات کو فیرومقناطیسی ریزوننس (FMR) کا استعمال کرتے ہوئے جانچا گیا۔ فلم کی موٹائیوں اور اینیلنگ پیرامیٹرز کی مکمل تحقیق کے ذریعے، ہم نے گلبرٹ ڈیمپنگ کانسٹنٹ میں نمایاں کمی حاصل کی، جس کی کم ترین ریکارڈ شدہ قیمت $\alpha = 2.1 \times 10^{-3}$ تھی۔

یہ تحقیق YIG پتلی فلموں کی بنیادی سمجھ میں اضافہ کرتی ہے اور اسپن پر بنی ٹیکنالوجیز کو آگے بڑھانے کے لیے ان کی صلاحیت کو اجاگر کرتی ہے۔ یہ نتائج مقناطیسی مواد کی کارکردگی کو بڑھانے میں بڑھوتری کے پیرامیٹرز پر عین کنٹرول کی اہمیت کو اجاگر کرتے ہیں۔ مزید برآں، تھیسس مستقبل کی تحقیق کی سمتوں کا خاکہ پیش کرتی ہے، جس میں انورس اسپن ہال ایفیکٹ (ISHE) کا مطالعہ شامل ہے، تاکہ YIG فلموں میں متحرکات کے بہتر ہونے کے عملی اثرات اور ممکنہ ایپلیکیشنز کو مزید دریافت کیا جا سکے۔

Contents

List of Figures

List of Tables

Chapter 1

Introduction

1.1 Literature Review

Spintronics, or spin-electronics, harnesses the spin degree of freedom of electrons for information processing and communication, offering a more power-efficient alternative to conventional electronics, which rely on electron transport and are prone to joule heating effects [1], [2]. The spin property unlocks a gateway to non-volatile memory, where data remains secure even if power is lost [2]. In spintronic devices, the spin orientations can be manipulated swiftly by various techniques such as applying magnetic fields, spin-polarized currents, or spin-orbit interactions, resulting in faster switching and data processing speeds [3]. In short, spintronic devices offer faster operation, cost efficiency,and surpass electronics in both scaling and high performance [2], [4].

To explore pure spin currents, it's necessary to employ a ferromagnetic (FM) material that is an electrical insulator [5]. In this setup, there is no transfer of electrical charge; instead, information is solely transmitted through spin waves. These spin waves, termed magnons, represent the quanta of spin waves and can travel extended distances, spanning up to centimeters, especially within materials exhibiting magnetic order.

Yttrium iron garnet (YIG) has garnered significant interest among researchers for its unique properties, making it an outstanding candidate for various spintronic and magnonic applications. The properties that make YIG the most widely studied magnetic material are its ferrimagnetic and electrically insulating nature at room temperature, high Curie temperature, ultra-low magnetic damping, low coercive field, remarkable chemical stability, long spin diffusion length, and ease of single-crystalline material synthesis [6], [7].

These properties of YIG have led to its widespread applications in various microwave devices, including oscillators, filters, and generators [8], [9]. As a ferrimagnetic insulator, YIG enables the generation of pure spin currents in magnon-based devices without requiring additional charge currents, thereby reducing power consumption [5], [7]. Its cubic crystal structure with Ia3d symmetry and extensive spin diffusion length make YIG well-suited for spin transport experiments [7], [9]. Additionally, YIG's exceptionally low Gilbert damping coefficient ($\alpha \approx 3 \times 10^{-5}$) and coercive field facilitate research into magnon dynamics, crucial for advancing spintronics applications [7]. This minimal damping is particularly beneficial for spin-torque oscillators and spin-wave-based logic circuits, highlighting YIG's central role in modern spintronics research and its potential for shaping future technologies.

Efforts have been made to grow nanometer-thick YIG films with properties comparable to bulk YIG, particularly focusing on achieving low Gilbert damping for spintronic and magnonic applications [8], [3]. Various methods such as molecular beam epitaxy (MBE), liquid phase epitaxy (LPE), magnetron sputtering and pulsed laser deposition (PLD) have been explored [9]. Among these, LPE is more suitable for micron-thick YIG films, while PLD and sputtering are better suited for nanometer-thick films. Significantly, sputtering offers advantages such as speed, reproducibility, cost-effectiveness, and scalability for large-scale industrial production [10].

1.2 Objectives

The primary goal of this thesis is to optimize the growth process of Yttrium Iron Garnet (YIG) thin films. The aim is to achieve the growth of monocrystalline YIG films with the smallest possible Gilbert damping constant. These optimized YIG films hold significant promise for advancing spintronics and magnonics applications, offering enhanced performance and functionality in these fields.

1.3 Structure of the Dissertation

In chapter two of this thesis, fundamental aspects of magnetization are explored, including topics such as exchange energy, the Landau-Lifshitz-Gilbert (LLG) equation, ferromagnetic resonance, as well as an in-depth examination of the crystal structure and magnetic properties of YIG.

Chapter three details experimental techniques for film preparation and its annealing, along with characterization methods for analyzing magnetic, structural, and morphological properties.

Chapter four is dedicated to the discussion of the dissertation's results.

Finally, the last chapter offers a conclusive summary of the research findings, accompanied by insights into potential future avenues for exploration.

Chapter 2

Comprehensive Review of Magnetism Associated with YIG

2.1 Introduction to Magnetism

The magnetic properties of materials stem from their atomic magnetic moment, primarily governed by the presence of unpaired electrons. When there is no external magnetic field, these electrons contribute to magnetism through two distinct mechanisms: orbital angular momentum, arising from their motion around the nucleus, and intrinsic magnetic moments due to their spin. The interplay between them is known as spin-orbit coupling and dictates the overall magnetic moment of the atom.

Additionally, the application of an external magnetic field induces a third contribution to the magnetic moment of a free atom, originating from alterations in the orbital angular momentum of electrons caused by the field. Understanding magnetic behavior at the atomic level is crucial for grasping the broader magnetic properties of materials [11].

2.1.1 Magnetic Moment

The magnetic moment of an atom arises from the combined contributions of its orbital and spin angular momenta. It is denoted by μ and serves as a fundamental property that characterizes the atom's response to an external magnetic field. The electron's total angular momentum, denoted as $\mathbf{J}$, is the combination of its orbital angular momentum $\mathbf{L}$ and its spin angular momentum $\mathbf{S}$. Mathematically, this relationship is expressed as:

$$\mathbf{J} = \mathbf{L} + \mathbf{S}. \tag{2.1.1}$$

The magnetic moment corresponding to this total angular momentum is expressed by the equation:

$$\boldsymbol{\mu} = -\gamma \mathbf{J}. \tag{2.1.2}$$

Here, $\gamma = \frac{g\mu_B}{\hbar}$ is called the gyromagnetic ratio. g is the electron g-factor (approximately equal to -2). $\mu_B = \frac{e\hbar}{2m_e}$ represents the Bohr magneton. e is the elementary charge, and m_e is the mass of the electron [6], [12].

2.1.2 Magnetization

Magnetization is a property of a material, dependent on the individual magnetic moments of its constituents (ions, atoms, and molecules), as well as their interactions. It quantifies the degree to which a material becomes magnetized when subjected to an external magnetic field. In mathematical terms, magnetization ($\mathbf{M}$) is expressed as the magnetic moment divided by the volume (V) [11].

$$\mathbf{M} = \frac{\boldsymbol{\mu}}{V}. \tag{2.1.3}$$

2.1.3 Magnetic Susceptibility

An important quantity indicating a material's response to an external magnetic field is its magnetic susceptibility. It represents the ratio of magnetization $\mathbf{M}$ to the external field $\mathbf{H}$ [11].

$$\chi = \frac{\mathbf{M}}{\mathbf{H}}. \tag{2.1.4}$$

Here, χ denotes magnetic susceptibility and $\mathbf{H}$ represents the external magnetic field. Materials with negative χ values are classified as diamagnetic, while those with positive χ values can exhibit paramagnetic, ferromagnetic, antiferromagnetic, or ferrimagnetic behavior.

2.1.3.1 Diamagnetism

The change in orbital motion due to the presence of external field results in diamagnetism. Diamagnetism is intrinsic to all materials even if the electron shells are completely filled. But this effect is so small that only the materials with filled electronic shells (having no net magnetic moment) show diamagnetism [11]. Diamagnetic materials are weakly magnetized in the direction opposite to the applied field.

2.1.3.2 Paramagnetism

Paramagnetic materials possess individual atomic magnetic dipole moments, leading to a collective magnetic dipole moment. However, these moments are weakly

coupled to each other, and thermal energy causes them to orient randomly, as illustrated in Figure 2.1. This orientation leads to a zero net magnetic moment when there's no external magnetic field. The susceptibility of paramagnetic materials has a small positive value, indicating weak magnetization along the direction of the externally applied field [11].

2.1.3.3 Ferromagnetism

Ferromagnets exhibit spontaneous magnetization below their Curie temperature. They feature a long-range alignment of atomic spins and magnetic moments, strongly interacting with each other through the exchange interaction. To minimize energy, ferromagnets undergo morphological division into small regions known as domains. Within each domain, all magnetic moments align parallel to each other, as illustrated in Figure 2.1. However, in the absence of an external field, different domains may have varying orientations, resulting in a zero net magnetization.
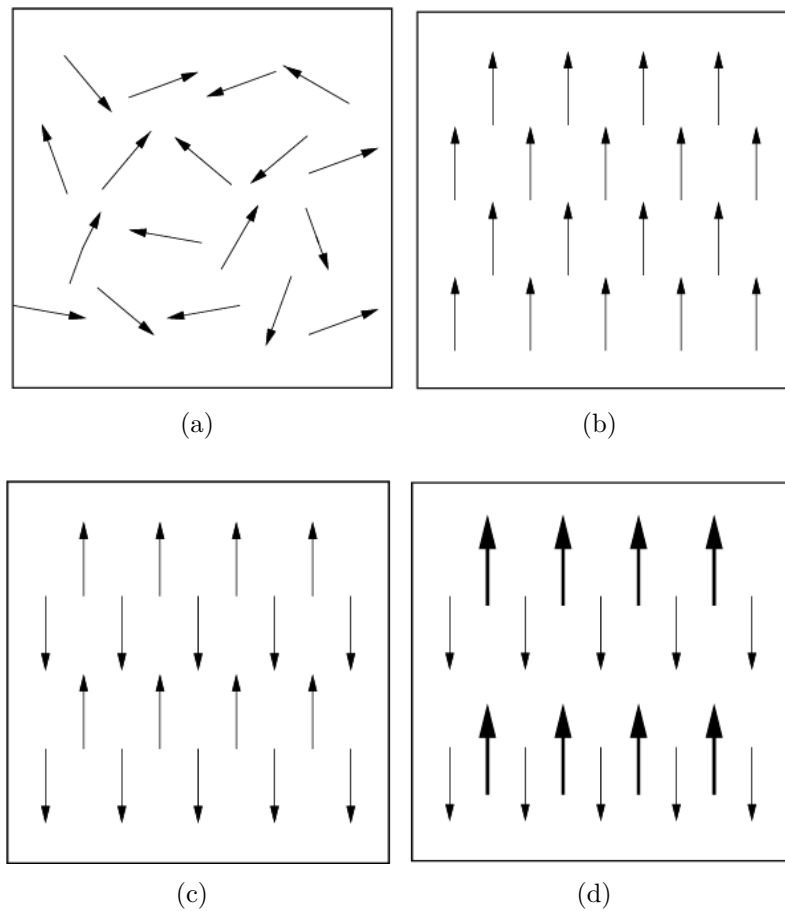
Figure 2.1: Illustration depicting different types of magnetism: (a) Paramagnetism, (b) Ferromagnetism, (c) Antiferromagnetism, and (d) Ferrimagnetism. Adapted from [11].

2.1.3.4 Antiferromagnetism

In antiferromagnets, the alignment of magnetic moments is antiparallel to each other, as illustrated in Figure 2.1, resulting in a zero net magnetization in the material.

2.1.3.5 Ferrimagnetism

In ferrimagnets, the dipoles align antiparallel to each other, but some dipoles are larger than others, as shown in Figure 2.1. As a result, the material exhibits a net magnetization, albeit smaller than in ferromagnets.

2.2 Exchange Energy

The exchange interaction has a quantum mechanical origin and arises as a consequence of the Pauli exclusion principle, which dictates that the total electronic wavefunction of a system must be antisymmetric. When two electrons have antiparallel spins, they are allowed to occupy the same atomic or molecular orbital. In this scenario, interchanging the electrons has no effect on the spatial part of the wavefunction, but it alters the sign of the spin part, maintaining overall antisymmetry. The total wavefunction, being a product of spin and spatial parts, always results in an opposite sign.

As a result of spatial overlap, these electrons experience increased Coulombic repulsion, leading to a higher energy state. Conversely, if the electrons have parallel spins, they must occupy different orbitals, reducing the Coulombic interaction and resulting in a lower energy state.

The exchange energy can be elucidated by solving the Schrödinger equation for a given system, such as the helium atom, as discussed in Spaldin's work [11]. In a quantum mechanical setup involving two atoms labeled as i and j, each possessing spins denoted by $\boldsymbol{S}_i$ and $\boldsymbol{S}_j$, the exchange energy is given by:

$$E_{\mathrm{exc}} = -2J\mathbf{S}_i \cdot \mathbf{S}_j. \tag{2.2.1}$$

In this expression, J signifies the exchange constant governing their interaction. For ferromagnetic materials, where J > 0, the exchange energy is minimized when the spins align in parallel to each other. Conversely, in antiferromagnetic materials, where J < 0, the antiparallel alignment of spins minimizes the exchange energy [12]. In addition to the exchange energy, other significant contributors to magnetic energy include magnetostatic energy, as well as magnetocrystalline and

magnetostrictive energies, highlighting the complexity and multifaceted nature of magnetic interactions in materials [11].

2.3 Magnetization Dynamics

When a magnetic moment is placed in an external magnetic field, the field tries to align the moment with its direction, resulting in a torque experienced by the dipole:

$$\boldsymbol{\tau} = \boldsymbol{\mu} \times \mathbf{B}_{\text{eff}}. \tag{2.3.1}$$

Since $\boldsymbol{\tau} = \frac{d\mathbf{J}}{dt}$, Equation (2.3.1) becomes:

$$\frac{d\mathbf{J}}{dt} = \boldsymbol{\mu} \times \mathbf{B}_{\text{eff}}. \tag{2.3.2}$$

Substituting Equation (2.1.2) into Equation (2.3.2), we obtain:

$$\frac{d\boldsymbol{\mu}}{dt} = -\gamma(\boldsymbol{\mu} \times \mathbf{B}_{\text{eff}}). \tag{2.3.3}$$

For a macroscopic system, the magnetic moment $\boldsymbol{\mu}$ can be replaced with the magnetization ($\mathbf{M}$) [12], and substituting $\mathbf{B}_{\text{eff}} = \mu_o \mathbf{H}_{\text{eff}}$ into Equation (2.3.3) yields an equation of motion for the magnetization:

$$\frac{d\mathbf{M}}{dt} = -\gamma(\mathbf{M} \times \mu_o \mathbf{H}_{\text{eff}}). \tag{2.3.4}$$

Here $\mathbf{H}_{\text{eff}}$ is the sum of all internal and external magnetic fields given by the following equation:

$$\mathbf{H}_{\text{eff}} = \mathbf{H}_o + \mathbf{H}_M(t) + \mathbf{H}_{\text{exc}} + \mathbf{H}_{\text{ani}} + \ldots \tag{2.3.5}$$

Here, $\mathbf{H}_o$ denotes the externally applied static magnetic field, $\mathbf{H}_M(t)$ represents the time-varying component of the applied magnetic field, $\mathbf{H}_{\mathrm{exc}}$ signifies the field arising from exchange interactions, $\mathbf{H}_d$ stands for the demagnetizing field, and $\mathbf{H}_{\mathrm{ani}}$ refers to the field resulting from shape and crystalline anisotropies [6].

According to Equation 2.3.4, the magnetization will precess indefinitely under the influence of the external effective field. This perpetual precession occurs at a frequency known as the Larmor frequency, $\omega = \gamma \mu_0 H_0$. Figure 2.2 provides a visual representation of this precession. For details, refer to [12].
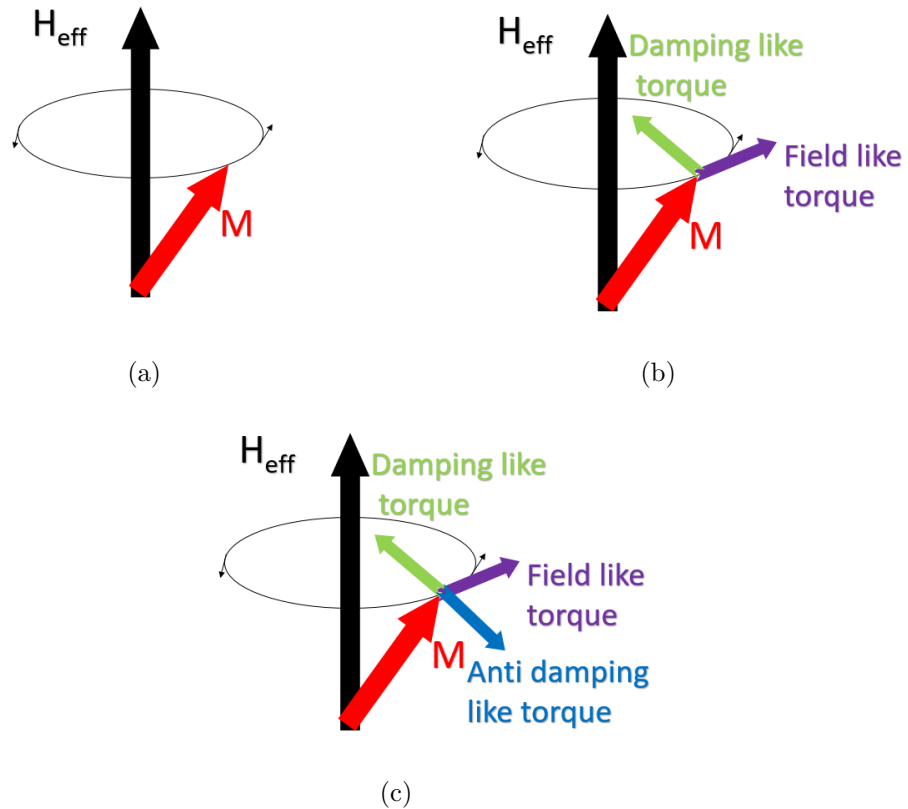
Figure 2.2: Dynamics of magnetization. (a) illustrates magnetization behavior without damping, (b) depicts magnetization dynamics with damping, and (c) demonstrates magnetization behavior with damping under the influence of an AC magnetic field.

However, this theoretical prediction contradicts experimental observations where magnetic damping occurs. In reality, the magnetization does not precess indefinitely; instead, it loses energy and eventually aligns itself with the external field,

as illustrated in Figure 2.2.

2.3.1 Landau-Lifshitz-Gilbert (LLG) Equation

To address damping effects, Landau and Lifshitz introduced a damping term to
Equation 2.3.3, resulting in the modified equation:

$$\frac{d\mathbf{M}}{dt} = -\gamma(\mathbf{M} \times \mu_o \mathbf{H}_{\text{eff}}) - -\frac{\lambda}{M_s}[\mathbf{M} \times (\mathbf{M} \times \mu_0 \mathbf{H}_{\text{eff}})], \qquad (2.3.6)$$

Here M_s denotes the saturation magnetization, and $\lambda = \frac{1}{\tau}$ represents the damping
constant corresponding to the relaxation time τ [6].

The opening term on the right side of Equation (2.3.6) signifies the precessional
torque, inducing magnetization precession around the external field. In contrast,
the subsequent term accounts for the damping torque, orthogonal to the preces-
sional torque, facilitating the magnetization's alignment with the external field.

In situations where damping is pronounced, Equation (2.3.6) suggests rapid preces-
sion of the magnetization. To provide a more accurate description of this behavior,
Gilbert introduced further adjustments in 1955. These refinements led to the de-
velopment of the Landau-Lifshitz-Gilbert (LLG) equation, represented by:

$$\frac{d\mathbf{M}}{dt} = -\gamma\mu_0 \mathbf{M} \times \mathbf{H}_{\text{eff}} + \alpha\frac{1}{M_s}(\mathbf{M} \times \frac{d\mathbf{M}}{dt}). \qquad (2.3.7)$$

This equation incorporates the effect of the dimensionless Gilbert damping param-
eter α, which characterizes the viscous nature of the damping mechanism [6]. The
parameter α governs the strength of the damping torque in the LLG equation,
influencing how rapidly the magnetization aligns with the effective magnetic field.
Higher values of α correspond to a stronger damping influence, underscoring the
system's tendency to dissipate energy as magnetization dynamics progress.

Equation 2.3.7 portrays the behavior of magnetization, illustrating a helical trajectory around the effective magnetic field, as depicted in Figure 2.2. This trajectory provides a realistic representation of magnetization's motion, characterized by damped precession. Such behavior underscores the intricate interplay between magnetization and the surrounding environment, particularly in the context of energy dissipation and spin angular momentum transfer.

The damping torque, highlighted by α in Equation (2.3.7), plays a pivotal role in facilitating energy dissipation and the transfer of angular momentum. Through spin-orbit interactions, this torque mediates the exchange of energy and spin angular momentum between the magnetization (manifested as magnon systems) and lattice vibrations (phonons). Essentially, the damping torque acts as a conduit through which the system dynamically interacts with its environment, revealing the complex relationship between magnetic phenomena and material properties.

2.3.2 Ferromagnetic Resonance

Ensuring that magnetization continues its precession around the external magnetic field requires replenishing the energy lost due to damping. This is typically achieved by employing an alternating current (AC) field orthogonal to the external magnetic field, often in the microwave frequency range as shown in Figure 2.2. When the precessional frequency of the magnetization aligns with the frequency of the AC field, a phenomenon known as ferromagnetic resonance occurs. During resonance, the magnetization absorbs maximum microwave energy.

The resonance frequency, where this synchronization occurs, is governed by Kittel's equation. Kittel's equation, a solution to the LLG Equation (2.3.4), offers a mathematical insight into the resonance frequency. This equation encapsulates various magnetic properties, including the gyromagnetic ratio γ, resonance field H_{res}, and effective magnetization M_{eff}. For a detailed derivation and discussion, refer to [12]. Mathematically, the resonance frequency is expressed as follows:

$$f_{\text{res}} = \frac{\mu_0 \gamma}{2\pi} \sqrt{H_{\text{res}}(H_{\text{res}} + M_{\text{eff}})}. \tag{2.3.8}$$

2.4 Detailed Examination of Yttrium Iron Garnet (YIG)

2.4.1 Crystal Structure of YIG

The crystal structure of YIG exhibits cubic symmetry with a lattice constant of 12.376±0.004 Å. It is classified under the space group $O_h^{10} - Ia3d$ [6], corresponding to space group number 230. Each unit cell comprises 160 ions, equivalent to 8 times the number of chemical formula units of $Y_3(Fe_2)Fe_3O_{12}$. Within the unit cell, there are three distinct types of sites: dodecahedral (c site), octahedral (a site), and tetrahedral sites (d site).
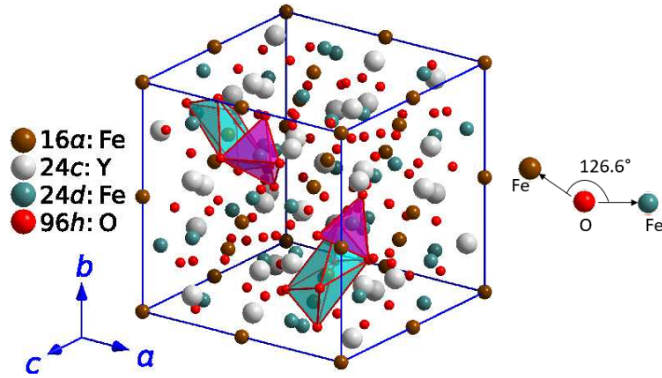
Figure 2.3: Crystal structure of YIG [6].

At the c site, the Y^{3+} cations are situated, each surrounded by eight O^{2-} ions, forming a dodecahedral configuration, as depicted in Figure 2.4. The lengths between Y^{3+} and O^{2-} are 2.37 Å and 2.43 Å [8]. The a sites hosts 16 Fe^{3+} cations, each encircled by six O^{2-} anions, creating an octahedral structure, as illustrated in Figure 2.4. The distance between octahedral site Fe^{3+} and O^{2-} is 2 Å [8]. The

remaining 24 Fe^{3+} cations occupy the d site, where each is encircled by four O^{2-} anions, resulting in a tetrahedral configuration (shown in Figure 2.4). The distance between tetrahedral site Fe^{3+} and O^{2-} is 1.88 Å [8]. All 96 O^{2-} ions occupy the general h sites, situated at the vertices of the dodecahedron, octahedron, and tetrahedron [6].

This arrangement of ions within the crystal lattice defines the unique structural characteristics of YIG, influencing its magnetic and optical properties.
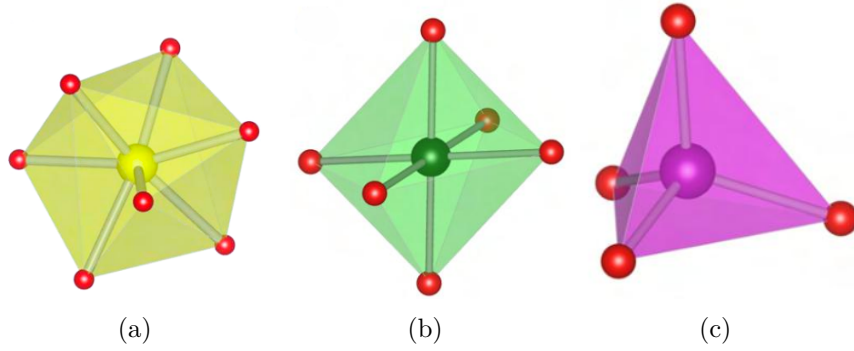

Figure 2.4: Oxygen ions as vertices of a (a) dodecahedron, (b) octahedron, and (c) tetrahedron.

2.4.2 Magnetic Properties of YIG

YIG exhibits a fascinating array of magnetic properties stemming from the intricate interplay of its atomic constituents and crystal structure. The interaction between O^{2-} and Fe^{3+} ions within the lattice serves as the basis for YIG's magnetic properties.

Y^{3+} ions, characterized by their closed-shell electronic configuration ($[Kr]4d^0 5s^0$), exhibit either non-magnetic or weak diamagnetic properties. In contrast, Fe^{3+} ions, each harboring unpaired 3d electrons, contribute a magnetic moment of 5μB, significantly influencing the material's overall magnetization.

The magnetization dynamics of YIG are governed by super-exchange interactions between Fe^{3+} ions across various lattice sites, facilitated by surrounding oxygen ions. Notably, Fe^{3+} ions at sites a and d demonstrate particularly strong magnetic

interactions, characterized by a $a - O^{2-} - d$ bond angle of 126.6 degrees [6].

The ferrimagnetic behavior in YIG is a consequence of the collective alignment of magnetic moments within its crystal structure. Specifically, within YIG's lattice, Fe^{3+} ions reside in two distinct sub-lattices: the tetrahedral and octahedral sites.

Initially, it's important to note that each Fe^{3+} ion within both the tetrahedral and octahedral sub-lattices favors parallel alignment of its magnetic moment with its neighboring ions. This preference mirrors the behavior typically associated with ferromagnetic materials, where neighboring magnetic moments align in the same direction.

However, the unique feature of YIG lies in the relative alignment between these two sublattices. While each sub-lattice individually tends to exhibit ferromagnetic-like behavior with parallel alignment, the orientations of the magnetic moments in the tetrahedral and octahedral sublattices are anti-parallel to each other.

This anti-parallel alignment preference between the sublattices causes certain magnetic moments to cancel each other out. As a result, YIG exhibits ferrimagnetism, with its net magnetic moment being determined by the difference between the magnetic moments of these sublattices.

2.4.3   Growth of YIG Thin Films on GGG (111) Substrates

To facilitate the epitaxial growth of yttrium iron garnet (YIG) thin films, researchers commonly employ (111) gadolinium gallium garnet (GGG) substrates. This choice is vital due to the alignment of GGG substrates with the easy magnetization axis of YIG. Such orientation compatibility ensures a favorable growth environment for YIG thin films, facilitating epitaxial growth and the development of desired magnetic properties.

GGG has a cubic crystalline structure, characterized by a lattice constant of 12.383 Å, closely matching that of YIG with a difference of just 0.01 Å. Additionally, the thermal expansion coefficient of GGG closely matches that of YIG [6], further

enhancing their compatibility.

In summary, the epitaxial growth of YIG thin films on (111) GGG substrates offers a highly effective approach to fabricate high-quality magnetic materials with controlled properties. This process capitalizes on the structural and thermal compatibility between the substrates, minimizing lattice mismatch and enabling precise control over film thickness and crystalline orientation.

Chapter 3

Experimental Methods

3.1 Magnetron Sputtering

Magnetron sputtering, a type of physical vapor deposition (PVD) method, is extensively employed in large-scale industrial manufacturing, particularly within the thin film industries, for depositing thin films onto substrates [6]. This technique, falling under the category of plasma deposition, involves the creation of plasma during the deposition process. Magnetron sputtering can be categorized into two types: Direct current (DC) and radio frequency (RF) sputtering. The former is utilized when the target material is metallic, while the latter is used for insulating target deposition.

In magnetron sputtering, a vacuum chamber houses various guns connected to either dc or RF power supplies. The material intended for deposition, referred to as the "target," is positioned on one of the guns and functions as a cathode, whereas the substrates are secured onto a sample holder acting as an anode. To achieve high-quality YIG thin films, a preferred configuration involves right angle deposition with a target-to-substrate distance ranging from 7 to 8 cm. Sputtering is conducted under high vacuum conditions, typically between 10^{-7} Torr to 10^{-8} Torr base pressures.
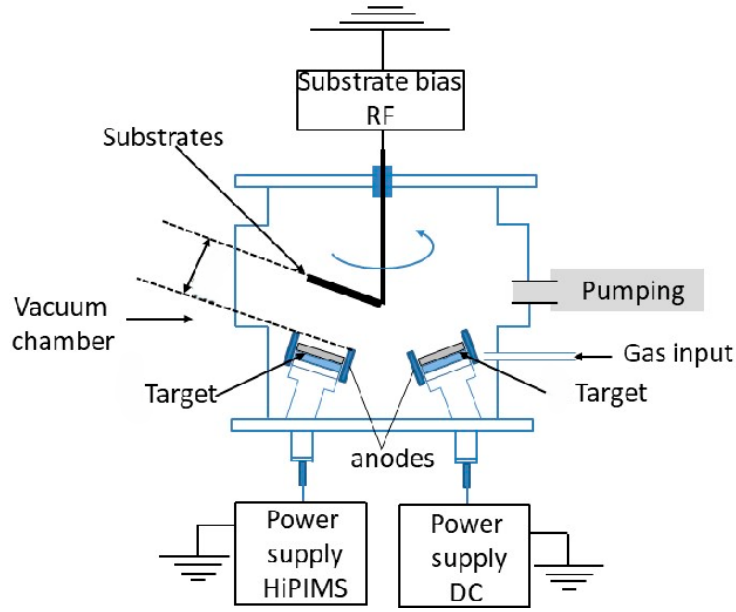
Figure 3.1: Schematic of magnetron Sputtering. The diagram illustrates magnetron sputtering setup with guns positioned at a 45° angle and a target to substrate distance of 8 cm.

Once the desired vacuum level is attained, argon gas is introduced into the vacuum chamber at low pressure, usually several milliTorr. Subsequently, a dc or RF power supply is activated and maintained at the required power level. The electric field within the chamber ionizes the argon atoms, generating plasma. Positively charged heavy argon ions are then attracted toward the negatively charged target. Through atomic collisions, some atoms are dislodged from the target and condense onto the substrate surface, forming thin films.

Beneath the target, permanent magnets are positioned to trap electrons via the Lorentz force. This action increases the collision rate and confines the plasma in the region between the target and substrate, thereby enhancing the sputtering rate.

3.1.1 Substrate Preparation

In this study, the Gallium Gadolinium Garnet (GGG, $Gd_3 Ga_5 O_{12}$) substrates with crystallographic orientation (100) and (111) were used. These substrates were 0.5 mm thick and had dimensions of 10×10 mm². Notably, the substrates featured a

polished surface on one side and a rough surface on the other. The polished side was designated for the deposition of YIG thin films.

Before cutting the substrate, it is necessary to keep the surface of the substrate safe from contamination. Hence the polished surface was spin coated using AZ 1512 HS positive photoresist at 4000 rpm spin speed for 1 minute, followed by a 3-minute soft baking period on a hot plate.

The substrates were then cut into multiple pieces using a Diamond Saw (SYJ – 150 Low Speed Diamond Saw) with diamond blades. The initial speed was 20 rpm and max speed was 30 rpm. The substrates are very delicate and require special care during the cutting process. They can even break in the cutting holder into unwanted shapes or sizes, hence it is very important to handle the cutting process with great care.

After the cutting process, all the substrates were separately cleaned in the ultrasonic bath in the following manner. First the substrates were dipped in acetone for 5 minutes in the sonicator, then for the next 5 minutes in isopropyl alcohol (IPA) and lastly for 5 minutes in distilled water.

3.1.2 Film Deposition

The magnetron sputtering system in our spin physics lab features three guns: two DC and one RF. These guns are positioned at 45°) angles. To facilitate right-angle deposition, the sample holder is also oriented at 45°), as illustrated in Figure 3.2. The YIG target with 99.99% purity was mounted on the RF gun. The GGG substrates along with Si(100) and Si/SiO$_2$, were attached to the sample holder 8 cm above the target, with the polished side facing the target, using double-sided carbon tape, as depicted in the Figure 3.3. The rotary pump was used to achieve the initial vacuum of about 10^{-3} Torr, then the turbo molecular pump was used to create the base pressure of about 4.1×10^{-7} Torr.
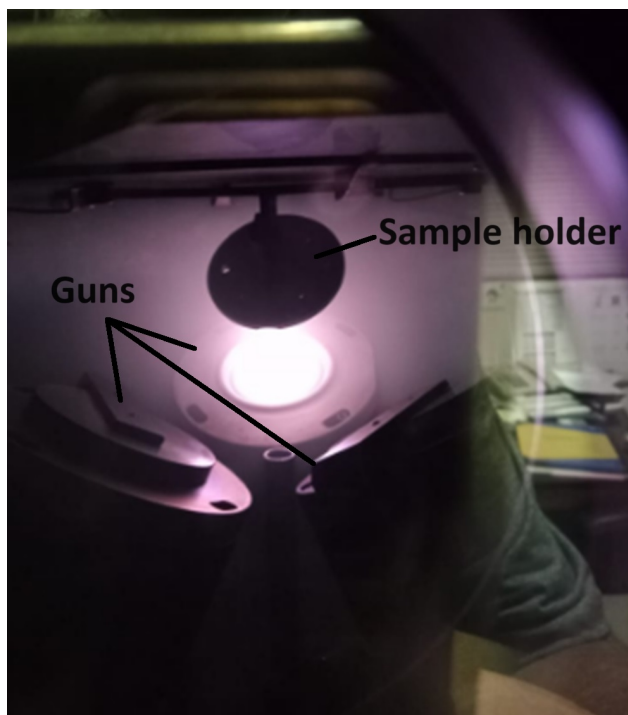
Figure 3.2: The diagram illustrates magnetron sputtering guns and sample holder at right angle to each other.

At the desired base pressure, the argon gas was introduced into the chamber, and the flow rate is maintained at 15 sccm from the control menu. It is called the working pressure. The RF power supply was turned on and ramp up gradually to 75 watts (absorbed power), the reflected power was zero. Reaching high power values abruptly is prohibited as it may damage the target. The target shutter is then opened.

Prior to deposition, it is good practice to clean the target by the process called pre-sputtering which is done by keeping the substrates shutter closed or rotating the substrates to the other side. Pre-sputtering helps get rid of surface impurities from the target.
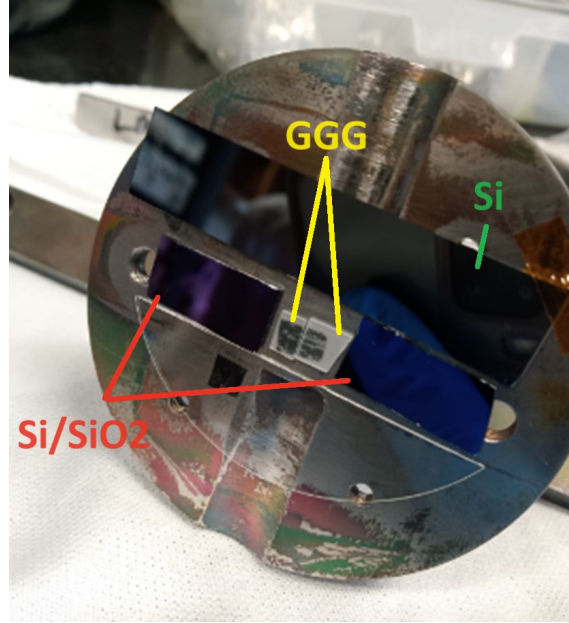
Figure 3.3: The diagram illustrates substrates attached to sample holder using double sided carbon tape.

The film thickness was estimated through various techniques such as "Ellipsometry and cross sectional Scanning Electron Microscopy (SEM). The deposition rates were then estimated by the sample thickness and deposition time, keeping all other conditions the same.

Table 3.1 summarizes the sputtering conditions during this research.

Parameter	Value
Base pressure	4.1×10^{-7} Torr
Argon flow rate	15 sccm
Radio frequency power	75 watt
Target to substrate distance	8 cm

Table 3.1: Details of the sputtering conditions.

3.2 Annealing Process for YIG Thin Film Crystallization

The as-deposited YIG thin film is amorphous and exhibits no magnetic response due to the presence of elements with different masses. Consequently, during the

sputtering process, different elements exhibit varying sputter rates, resulting in an amorphous form [6], [7]. This lack of crystallinity is why the films show no magnetic response. To attain a crystalline structure of YIG along the GGG crystalline planes, it is suggested to anneal the samples, preferably in an oxygen environment. The oxygen environment is crucial because it helps fill any oxygen vacancies present within the structure [6].

The samples were placed on a ceramic boat inside the vacuum tube furnace , as illustrated in figure 3.4. Oxygen flow was controlled by a digital mass flow controller. The samples underwent heating at a specific temperature, referred to as the annealing temperature, for a fixed duration known as the annealing time. The annealing temperature, annealing time, and oxygen flow rate were varied during this study.
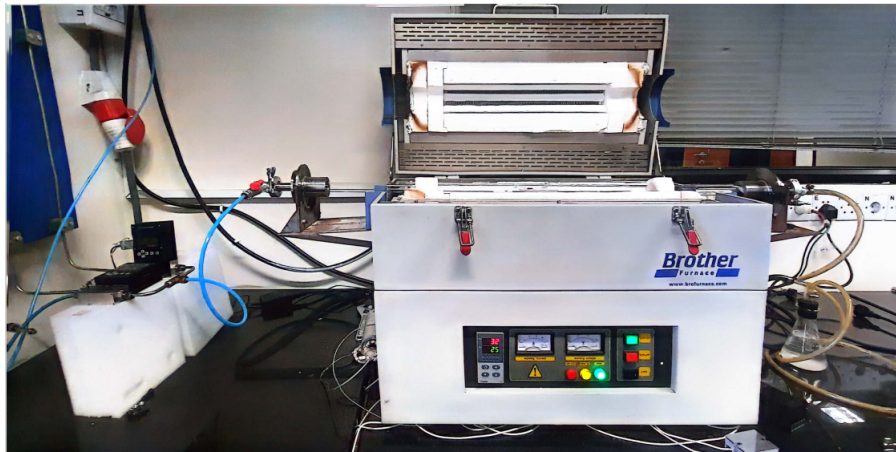

Figure 3.4: Vacuum tube turnace.

The heat treatment was performed in the following way:

Initially, the temperature was gradually increased to the desired level over a span of 2 hours. Subsequently, the temperature was sustained for the specified annealing time. Finally, the temperature was gradually reduced back to room temperature over a duration of 12 hours, as depicted in the Figure 3.5.
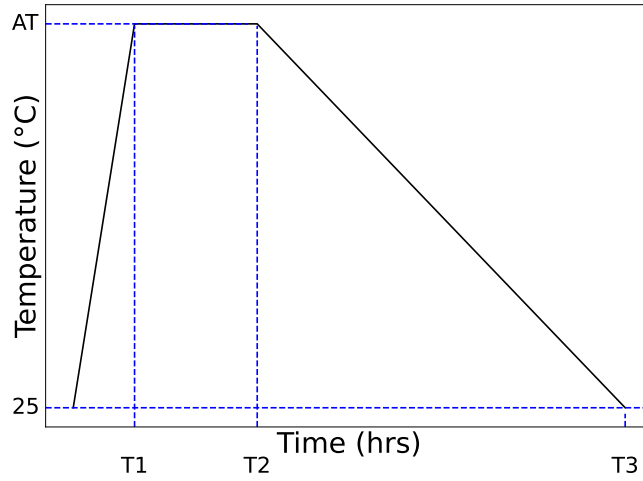
Figure 3.5: The graph illustrates the annealing process over time, depicting the variation in temperature. The dashed lines represent specific annealing steps labeled as T1, T2, and T3, while AT represents the annealing temperature.

Following the heat treatment, a noticeable change occurred in the color of the samples, rendering them more transparent. This alteration can be considered the first indication of a crystallographic phase change.

3.3 Ferromagnetic Resonance (FMR) Technique

Ferromagnetic resonance (FMR) is a potent experimental technique utilized extensively in the investigation of magnetic materials. It serves as a robust tool for exploring magnetic phenomena such as magnetic anisotropy, exchange interactions, and damping effects, providing invaluable insights into the fundamental physics governing magnetization dynamics [11].

By exposing a sample to a fluctuating magnetic field while simultaneously irradiating it with microwaves, FMR reveals important magnetic properties such as the resonance field, linewidth, and damping constant. The resonance field corresponds to the magnetic field strength at which the magnetization of the material absorbs energy most efficiently from the microwave radiation [12], [6]. The linewidth provides information about the width of the resonance peak, which is influenced by

24

factors such as magnetic anisotropy, exchange interactions, and damping. The damping constant characterizes the rate at which the magnetization relaxes to its equilibrium state, reflecting the energy dissipation mechanisms within the material. In various fields, ranging from magnetic recording to spintronics and magnetic sensor technologies, FMR finds widespread applications. Notably, in the analysis of thin films, two primary experimental techniques are commonly employed: vector network analyzer ferromagnetic resonance (VNA-FMR) and lock-in ferromagnetic resonance (Lock-In FMR).

3.3.1   Vector Network Analyzer (VNA)-Based FMR

A typical setup for a vector network analyzer (VNA) involves a microwave energy source, which serves as both a generator of the AC field and a detector, connected to a sample via a transmission line such as a stripline or coplanar waveguide (CPW) as illustrated in Figure 3.6. The sample, mounted on the stripline or CPW, is then positioned within the external static magnetic field, as depicted in the accompanying Figure 3.6. The source generates an ac field orthogonal to the static field, exciting the sample, while the detector records the power that is reflected or transmitted following interaction with the sample. By analyzing the reflectance or transmittance, which represents the ratio of reflected or transmitted power to the incident power, the scattering parameters (S11, S22, S12, S21) can be derived (see [12] for more details). These parameters offer insights into the properties of the sample, facilitating the extraction of relevant characteristics and behaviors.
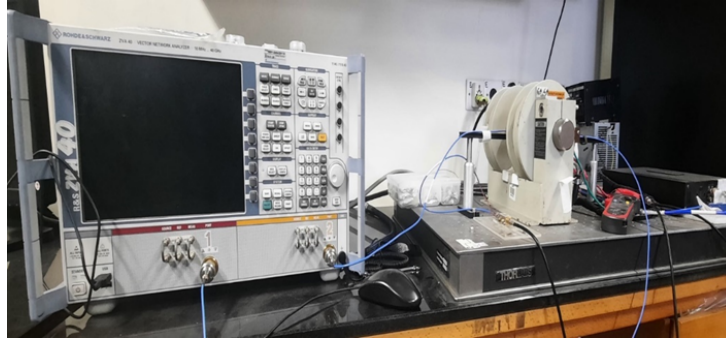
(a)
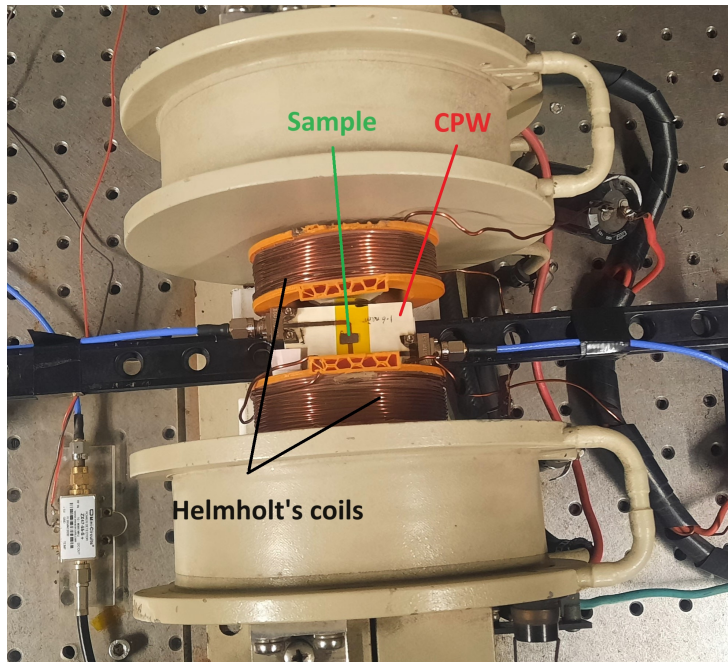
(b)

Figure 3.6: Vector network analyzer (VNA) setup: (a) VNA equipment and (b) sample placed on the stripline inside an external magnetic field.

3.3.1.1 FMR Data Acquisition

The entire setup is connected to a computer and controlled by a Python script. It allows for either frequency-swept Ferromagnetic Resonance (FMR) or field-swept FMR experiments.

In the field-swept FMR mode, the frequency is maintained constant at a particular value, while the external static field is varied across a desired range to identify the resonance field for that frequency [12]. The Python code and its functionality

are detailed in [13]. The code prompts you to input lower and upper bounds for frequency and field values. It then increments the frequency in equal steps, determines the resonance field for each frequency value, and generates an unfiltered 2D color plot illustrating the relationship between frequency and resonance field.

3.3.1.2 Filtering FMR Data

To clean the data and remove noise, different filters such as Gaussian, Median, and Spline can be applied. These filters enhance the accuracy and clarity of the resulting 2D density plot by mitigating the effects of random noise and other irregularities in the data. The improved plot, which provides a clearer visual representation of the relationship between frequency and resonance field, is illustrated in Figure 3.7. For a comprehensive explanation of the filtering process, see [13].
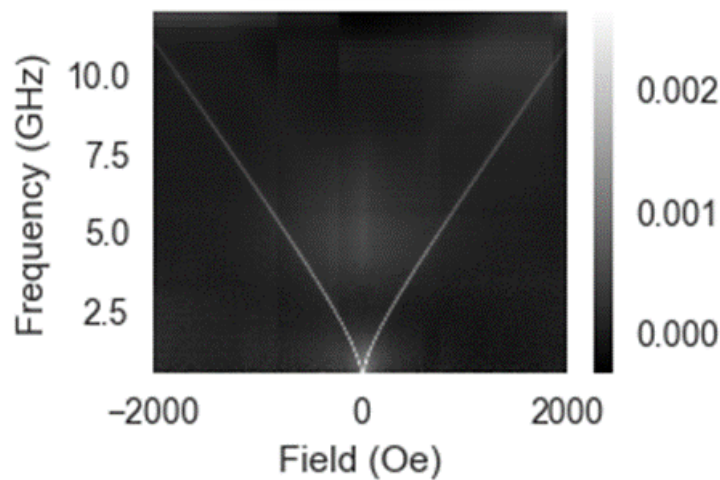

Figure 3.7: VNA-FMR color plot of frequency vs resonance field.

Similarly, in frequency-swept FMR mode, the static field is held constant while the frequency is swept across a range to identify the resonance frequency for each field value.

Utilizing the Python script in [13], linewidth at different frequency values can be extracted. Additionally, it also plots how the resonance field shifts with varying

frequencies as demonstrated in Figure 3.8.
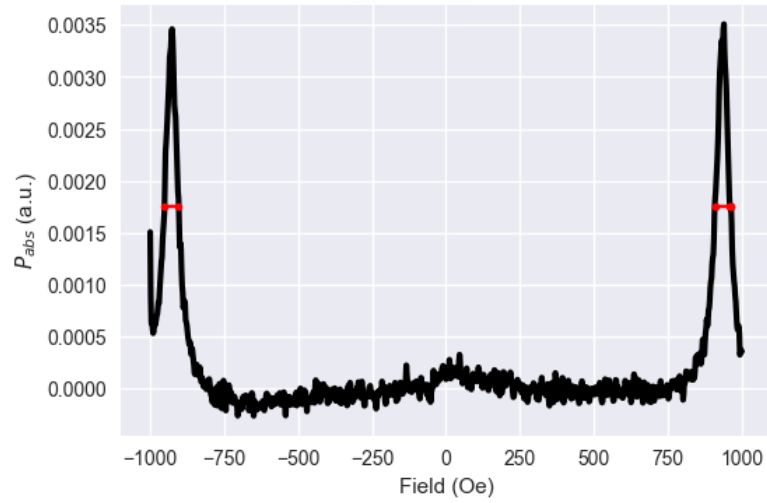
(a)
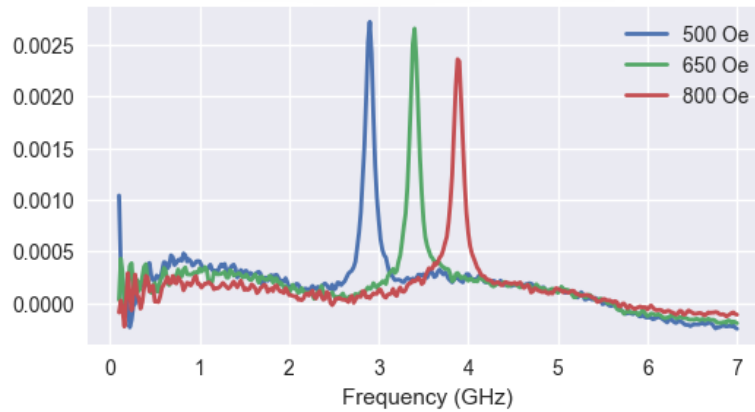
(b)

Figure 3.8: Resonance field and linewidth analysis. (a) Plot showing linewidth variations at different frequency values. (b) Graph illustrating the shift in resonance field with varying frequencies.

3.3.1.3 Model Fitting of FMR Data

To obtain the linewidth and resonance field for a range of frequency values, the derivative of magnetization $(\frac{dP}{dH})$ with respect to the external field is measured. The process of model fitting for FMR data is detailed in [14]. The Python script loads the data files and applies model fitting techniques to analyze them.
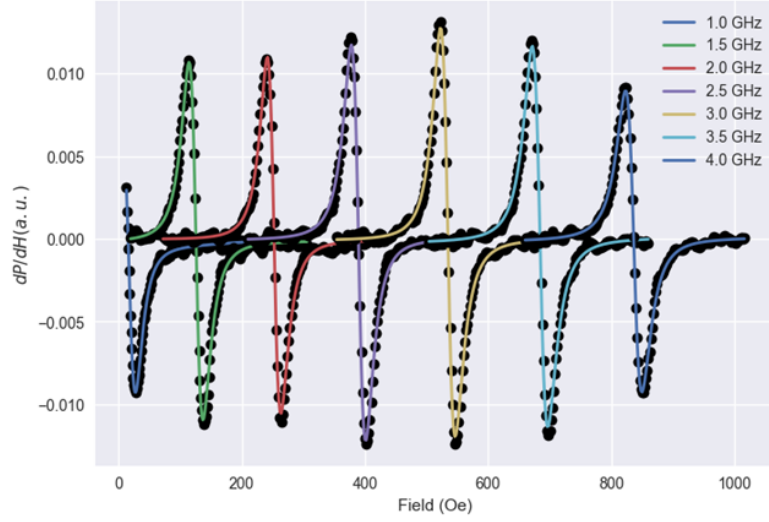
Figure 3.9: Color plot depicting $\frac{dP}{dH}$ at different frequency values vs field.

The Gilbert damping constant α can be calculated from the linewidth using the relation:

$$dH = \frac{4\pi\alpha f}{\gamma\mu_0} \tag{3.3.1}$$

The code applies linear regression to plot linewidth against frequency and extracts the Gilbert damping constant (α). This method allows for a precise determination of α by analyzing the slope of the linear fit, thereby providing crucial insights into the magnetic damping properties of the material.
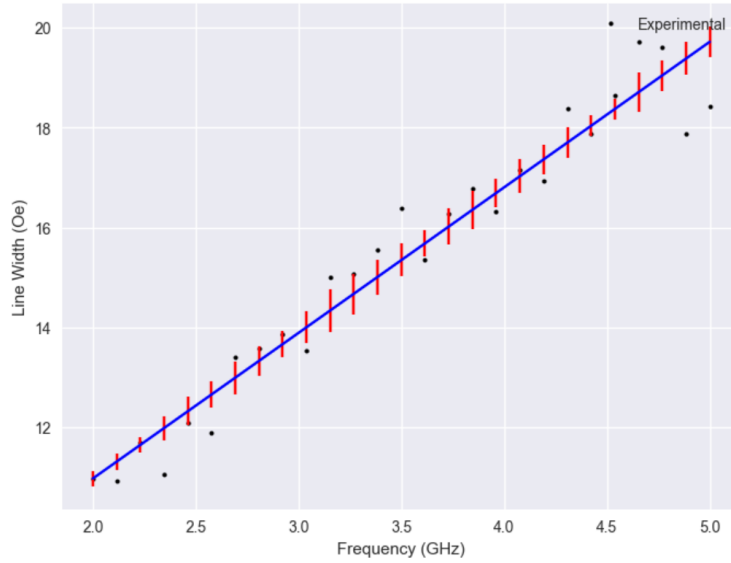
Figure 3.10: Linewidth vs. frequency with linear fitting. The plot displays the experimental values obtained from the analysis (dots) and the corresponding linear fit (solid line), used to extract the Gilbert damping constant (α).

3.4 Magneto-Optic Kerr Effect

The magneto-optical Kerr effect (MOKE) is an experimental technique that is used to investigate the magnetic characteristics of materials using polarized light. In this method, polarized light interacts with a magnetized material and encounters a change in its polarization upon reflection, which can be utilized to ascertain the magnetic characteristics of the material. It is particularly useful for studying magnetic domains, domain wall motion, magnetic anisotropy, and magnetization reversal.

In MOKE experiment, the sample is placed between the poles of an alternating electromagnet. This electromagnet, controlled to alter the sample's magnetization, applies a time-varying magnetic field to the sample. By rapidly switching the direction or amplitude of the magnetic field, the magnetization of the sample can be dynamically modified. This dynamic modulation allows for the study of time-dependent magnetic phenomena, such as magnetic domain dynamics and magnetization reversal processes.

In a typical MOKE setup, unpolarized light from a laser source passes through a polarizer before being incident on the sample. The polarized light interacts with the sample's magnetic moments, resulting from the alignment of electron spins within the atoms. This interaction causes the Zeeman effect (splitting of energy levels within the material in the presence of a magnetic field), which leads to changes in the polarization state of the light.

The alteration in the polarization state of light following reflection from a magnetized surface is termed Kerr rotation. This rotation occurs because the plane of polarization of the reflected light is influenced by the orientation of the magnetic moments within the material. The reflected light then passes through another polarizer before reaching the detector. The extent of polarization change provides information about the magnetic properties of the material.

In addition to the basic setup, a modulator and a lock-in amplifier are employed. The modulator introduces a periodic variation in the intensity or polarization of the incident light, while the lock-in amplifier synchronizes with the modulation frequency to selectively detect the signal corresponding to the MOKE response. This technique enhances the signal-to-noise ratio and enables sensitive measurement of the magneto-optical signal, particularly in noisy environments.

MOKE can manifest in three different geometries, as depicted in Figure 3.11:

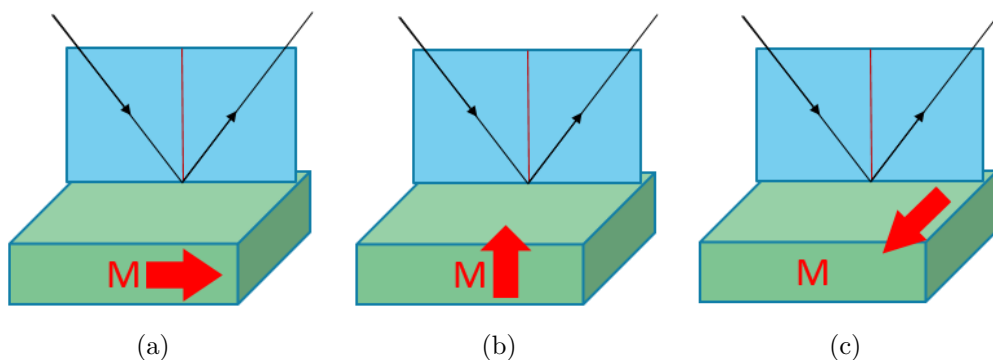(a)   (b)   (c)

Figure 3.11: MOKE geometries: (a) longitudinal MOKE, (b) polar MOKE, and (c) transverse MOKE.

Longitudinal MOKE (L-MOKE): In this configuration, the magnetization of the material is parallel to both the plane of sample and the plane of incidence.

Polar MOKE (P-MOKE): Here, the magnetization is parallel to the plane of incidence but orthogonal to the plane of the sample.

Transverse MOKE: This geometry involves magnetization orthogonal to both the plane of the sample and the plane of incidence.

L-MOKE measurements were conducted for all samples using a laser with a wavelength (λ) of 405 nm. To enhance the signal-to-noise ratio, 30 scans were performed for each sample, and the average of these scans was plotted. Figure 3.12 compares the hysteresis loops obtained from MOKE analysis of a single scan with those from an average of 30 scans.
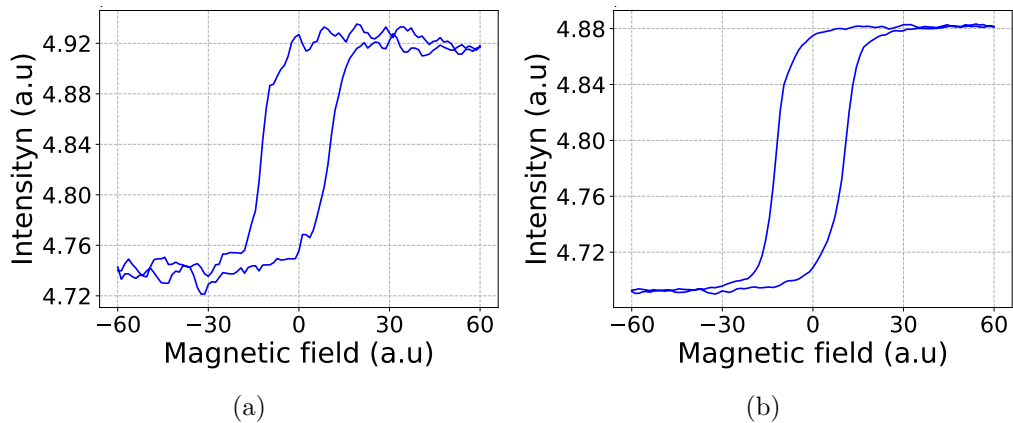

(a)

(b)

Figure 3.12: Comparison of hysteresis loops for YIG films: (a) single scan and (b) average of 30 scans.

3.5   Vibrating Sample Magnetometry (VSM)

Vibrating sample magnetometry (VSM), also known as a Foner magnetometer, is a widely used scientific apparatus utilized for gauging the magnetic characteristics of materials. It is particularly useful for studying the magnetic behavior of thin films, nano particles, and other small-scale samples. Its operational foundation lies in Faraday's law of electromagnetic induction.

Figure 3.13 illustrates the main components of a VSM setup. In a typical configuration, the sample under investigation is mounted on a mechanical oscillator and placed in a constant external magnetic field. If the sample exhibits magnetic properties, it becomes magnetized in alignment with the external field. The sample's dipole moment then generates a magnetic field around it known as the stray field [6].

Surrounding the sample are coils, referred to as pick-up coils, positioned in close proximity. The mechanical oscillator induces an up-and-down vibration of the sample with a constant amplitude. This motion causes a changing magnetic flux to pass through the pick-up coils.

Following Faraday's law of electromagnetic induction, a fluctuating magnetic flux generates an electric current in the pick-up coils. The magnitude of this current correlates directly with the magnetization of the sample [6]. To measure this current accurately, a lock-in amplifier is utilized, providing precise recordings of the sample's magnetization as a function of the applied magnetic field.
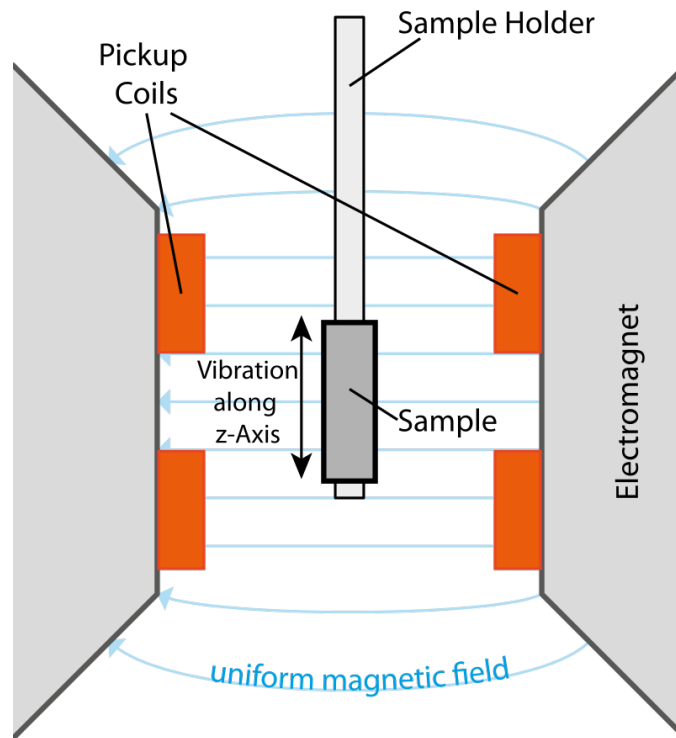
Figure 3.13: Schematic of VSM.

The VSM analysis was conducted at room temperature for all samples. Due to the larger volume of the substrates (GGG), the paramagnetic response dominated in the samples. To isolate the magnetic response of the films, the magnetic response of the substrate was subtracted from the samples. Figure 3.14 compares the VSM analysis of the samples with and without the substrate response.
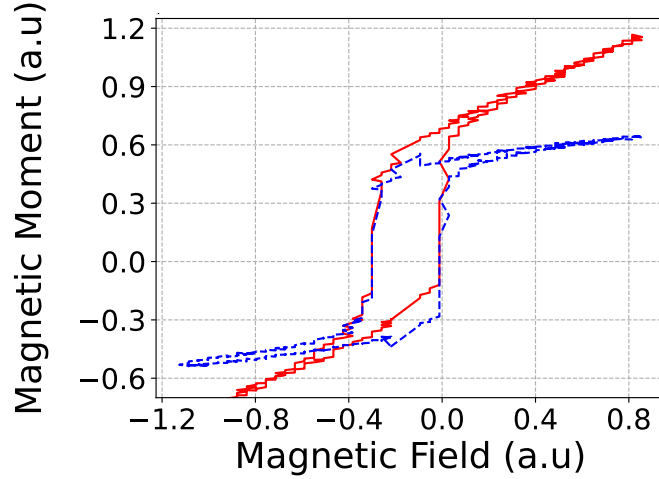
Figure 3.14: Hysteresis loop comparison of YIG films: the hysteresis loop with the solid line represents the magnetic response of YIG with the GGG substrate, while the hysteresis loop with the dotted line represents the magnetic response of YIG without the GGG substrate.

3.6 X-ray Diffraction (XRD)

Crystallographic analysis were carried out using X-ray diffraction (XRD). XRD is a powerful technique that is used to study the arrangement of atoms in crystalline materials. It utilizes X-rays being diffracted from electron dense regions, providing key information about the lattice parameters, crystal orientation, and to detect any lattice mismatches or defects present in the thin films.

When X-rays of wavelength comparable to atomic spacing are incident on crystals, they get scattered from different crystallographic planes and diffraction patterns are observed. For constructive interference to occur, the scattered waves must satisfy the Bragg's condition:

$$2d \sin \theta = n\lambda \tag{3.6.1}$$

Where d represents the distance separating adjacent diffracting lattice planes, θ denotes the angle of incidence of X-rays on the crystal planes, n signifies the diffraction order, and λ stands for the wavelength of the incident X-rays.

Chapter 4

Results and Discussions

In this chapter, we delve into a comparative analysis of the XRD, VNA-FMR, MOKE, and VSM results obtained from YIG thin films grown on GGG(100) and GGG(111) substrates. Our primary aim is to optimize the growth conditions of these YIG thin films in order to minimize the Gilbert damping constant. To achieve this goal, we systematically varied parameters such as annealing time, annealing temperature, and film thickness/deposition time. Table 4.1 provides a summary of the investigated samples, including their deposition time and annealing parameters.

Sample name	Sample description	Deposition time (min)	Annealing Temperature (°C)	Time (hrs)	Alpha (α)
Sample 1	YIG/GGG(100)	62	800	4	$5.6 \times 10^{-3}\,(0°)$ $7.6 \times 10^{-3}\,(90°)$
Sample 2	YIG/GGG(111)	62	850	4	——
Sample 3	YIG/GGG(111)	62	800	4	3.2×10^{-3}
Sample 4	YIG/GGG(111)	31	800	6	3.1×10^{-3}
Sample 5	YIG/GGG(111)	31	900	6	2.1×10^{-3}
Sample 6	YIG/GGG(111)	15.5	900	6	——

Table 4.1: Annealing parameters and corresponding Gilbert damping constant (α) for investigated samples.

4.1 XRD Analysis of YIG films

Figure 4.1 compares the XRD peaks of the annealed and unannealed samples, illustrating that after annealing, the peak intensities enhance, and some peaks emerge that were absent in the unannealed samples. The unannealed samples exhibited no magnetic response, suggesting their amorphous nature. However, after annealing, the samples exhibited a magnetic response, indicating a transition to a crystalline structure.
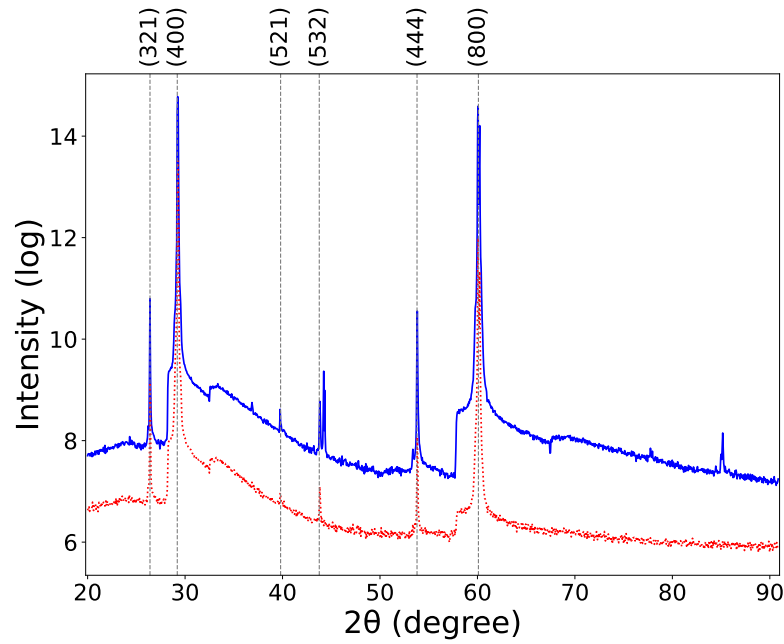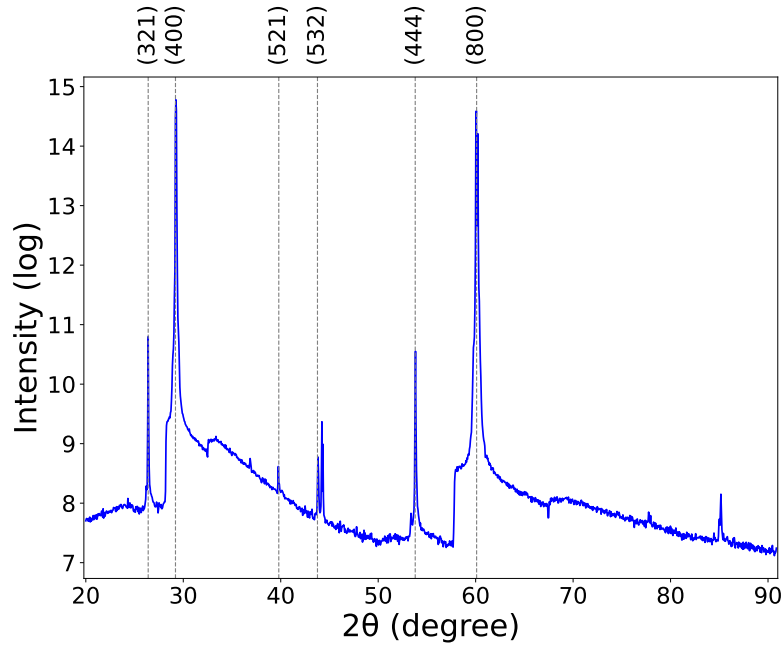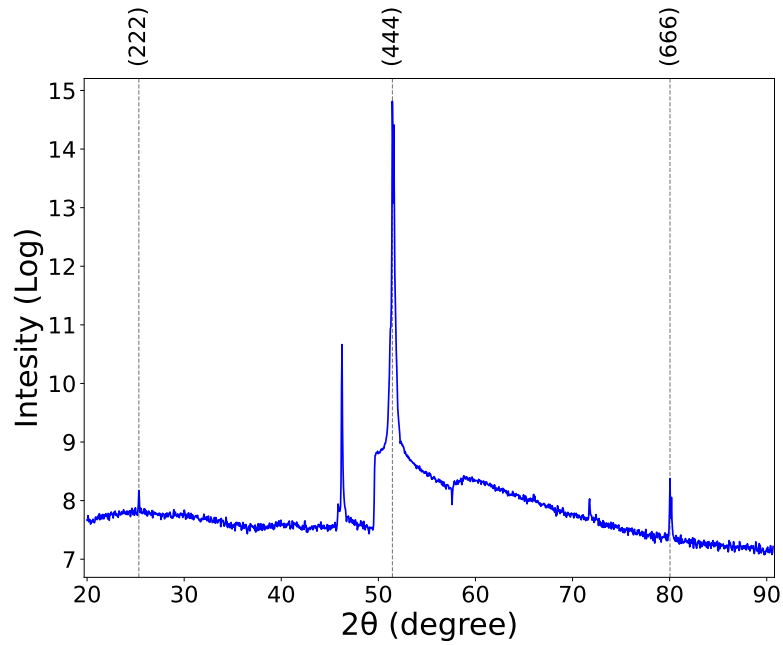

Figure 4.1: XRD analysis of YIG on GGG(100) illustrating the changes in peaks before (dotted line) and after (solid line) the annealing process.

Figure 4.2 displays the XRD spectra obtained from YIG films grown on GGG substrates with crystallographic orientations (100) and (111) post-annealing.

Figure 4.2: Post annealing XRD spectra of a) YIG on GGG(100) and b) YIG on GGG(111).

As the lattice parameter of YIG and GGG exhibit a slight difference of approximately 0.01 Å, their diffraction peaks are very closely spaced. In order to resolve these peaks and analyze their characteristics accurately, a slow scan was conducted.

Figure4.3 unveils the resultant XRD profiles, obtained from the slow scan.
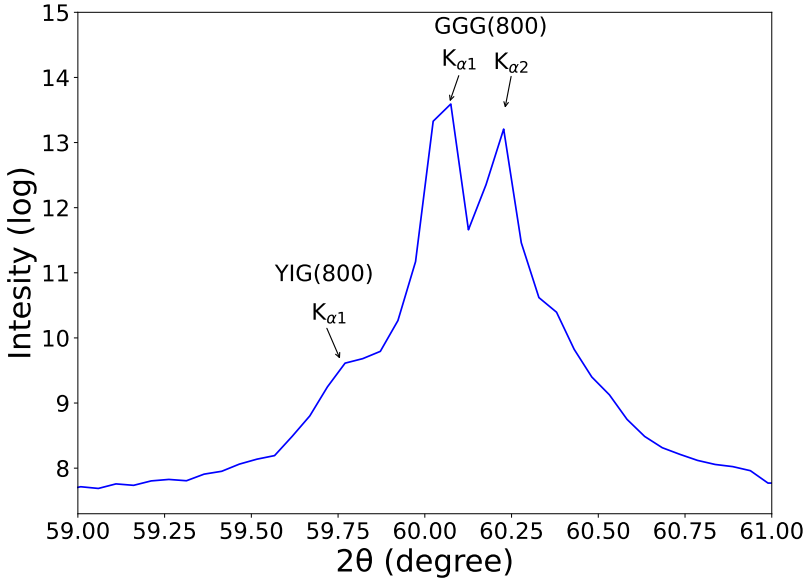
(a)
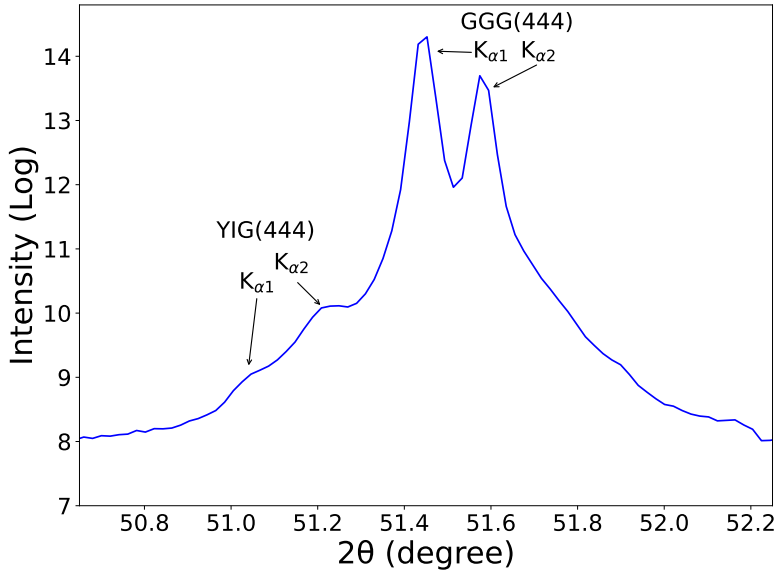
(b)

Figure 4.3: Slow scan illustrating (a) peaks from the (800) family of planes of YIG on GGG(100) and (b) peaks from the (444) family of planes of YIG on GGG(111).

4.2 VNA-FMR Characteristics of YIG films

Anisotropy was induced in the YIG films deposited on GGG substrate oriented along the (100) direction by affixing magnets to the substrate holder, where the substrate was positioned. This technique facilitated the alignment of magnetic moments along the direction of the applied magnetic field. As a result, the magnetic domains exhibited a preferred alignment direction rather than random orientations. It is important to note that no magnets were used during the deposition of YIG films on GGG(111) substrates. Consequently, these samples do not exhibit induced anisotropy.

When analyzing the sample (YIG on GGG(100)) with VNA-FMR, measurements were first taken along the easy axis, which is the direction where the magnetization aligns most easily. This axis is labeled as zero degree. Subsequently, measurements were conducted along the hard axis, by orienting the sample 90 degrees, where the magnetization is less prone to aligning and labeled as 90 degree.

In panels a) and b) of Figure 4.4, we observe distinct behaviors reflecting the anisotropic properties of the YIG film on GGG(100) substrate.

Panel a) showcases the magnetization response along the easy axis. Here, as the external magnetic field direction changes, the magnetization smoothly adjusts to align with it. This smooth transition indicates the ease with which the magnetization direction can be altered along the preferred axis.

Conversely, in panel b), we explore the magnetization behavior along the hard axis. Unlike the smooth transition observed in panel a), the magnetization here does not smoothly transition with changes in the external magnetic field direction. Instead, it exhibits discrete changes, suggesting a higher energy barrier to reorient magnetic moments along this less favorable axis. This phenomenon underscores the preference of magnetic moments to align along the easy axis and the additional energy required to alter their orientation along the hard axis.
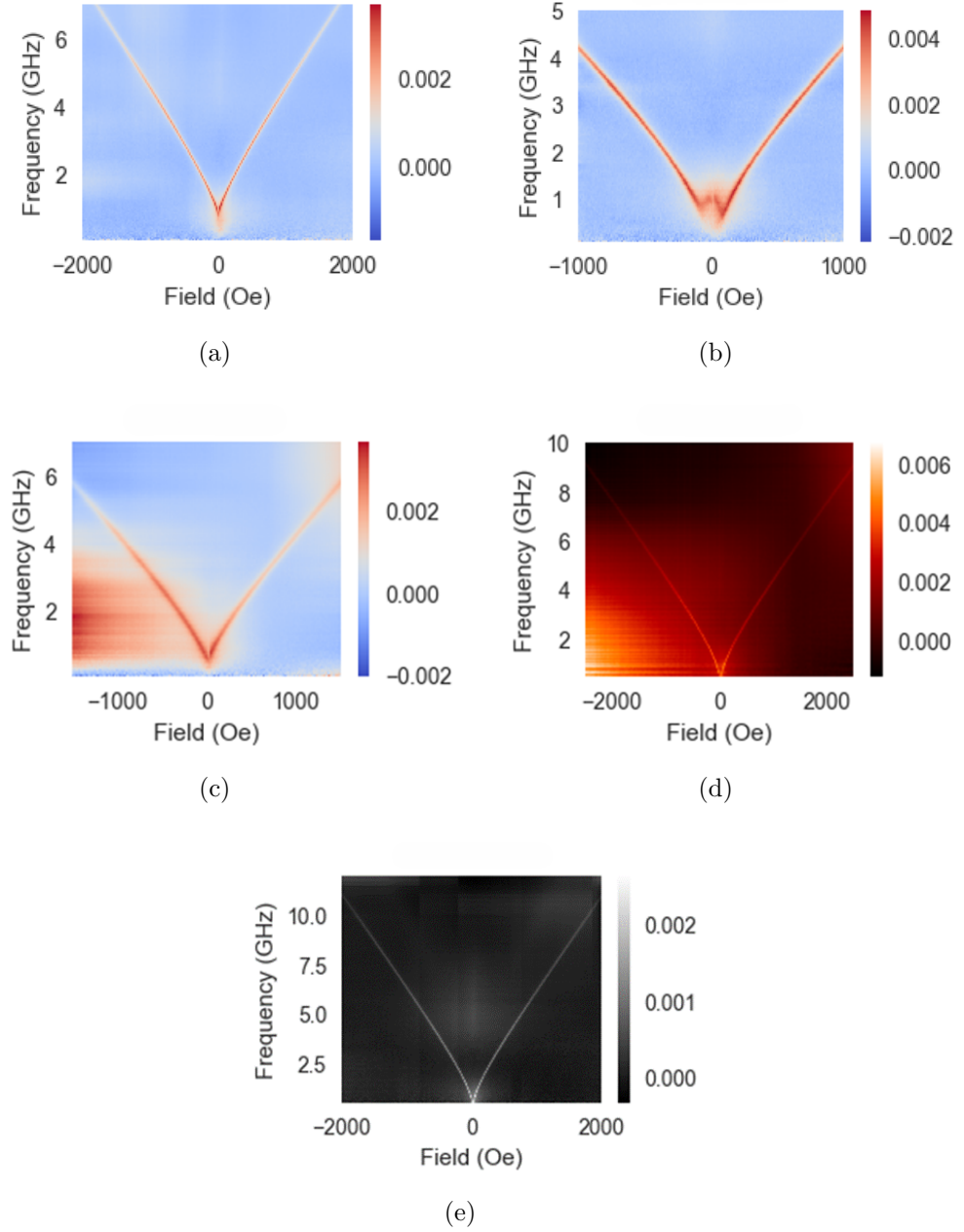
Figure 4.4: Field swept VNA-FMR of a) sample 1 at 0°), b) sample 1 at 90°), sample 3, d) sample 4, and e) sample 5 (see Table 4.1 for sample details).

Figure 4.4 displays the VNA-FMR color plots of various YIG samples with different thicknesses and annealing parameters. Comparing their frequency against resonance field spectrum reveals the influence of thickness and annealing parameters on the magnetic response of the samples. The resonance peaks sharpen progressively from sample 1 to sample 5, suggesting increased crystallinity, reduced linewidth,

lower Gilbert damping constant (as evident from Table 4.1), and enhanced homo-
geneity of magnetic moments.

4.3   MOKE Analysis of YIG films

Figure 4.5 illustrates the MOKE analysis of samples with varying thicknesses and
annealing parameters. The hysteresis curves depicted in the figure showcase the
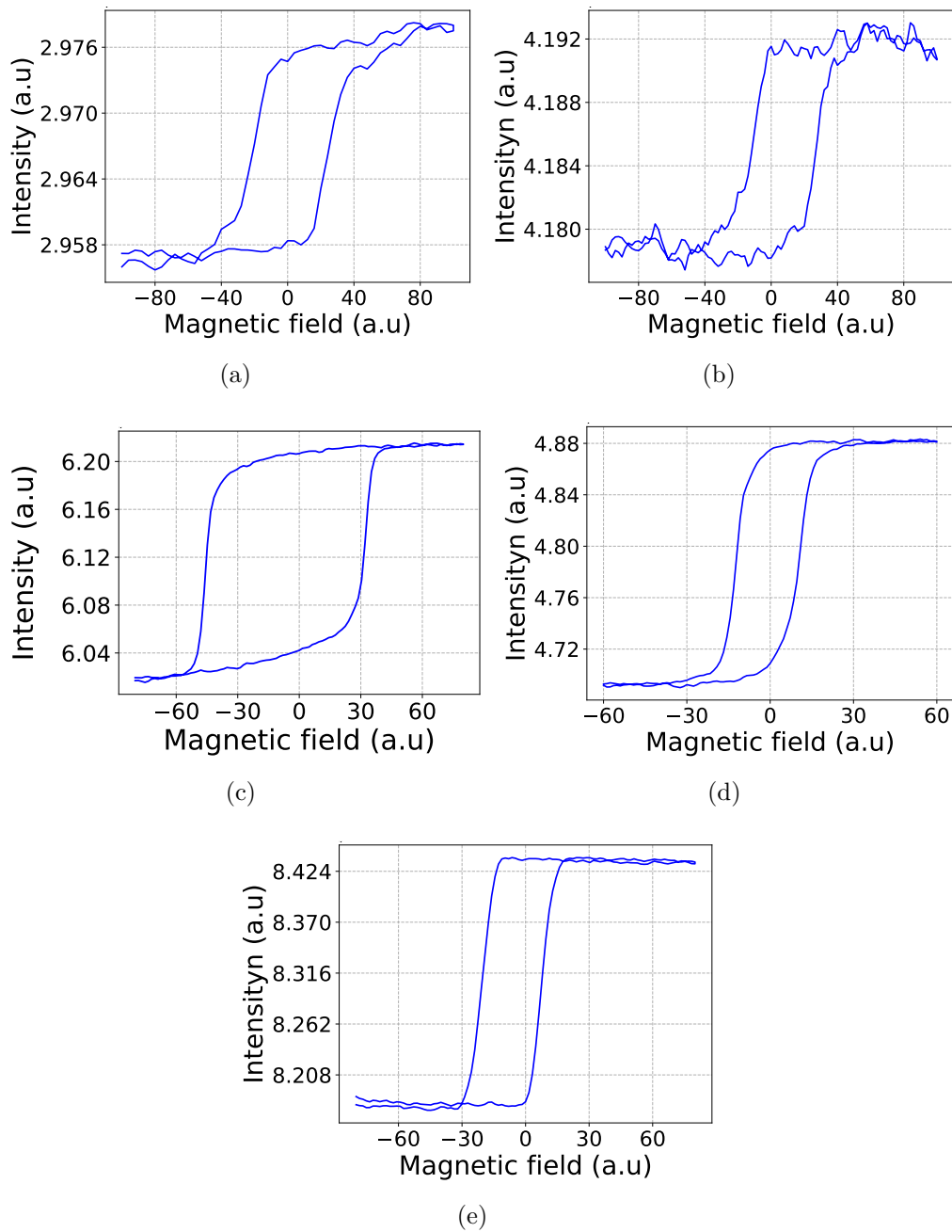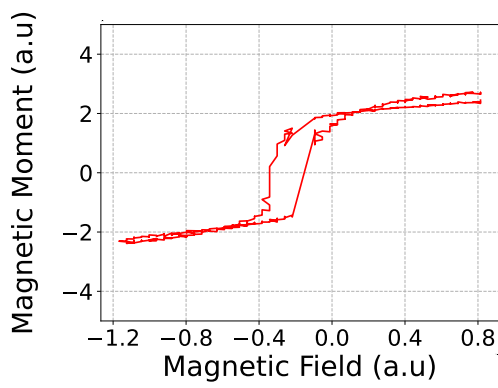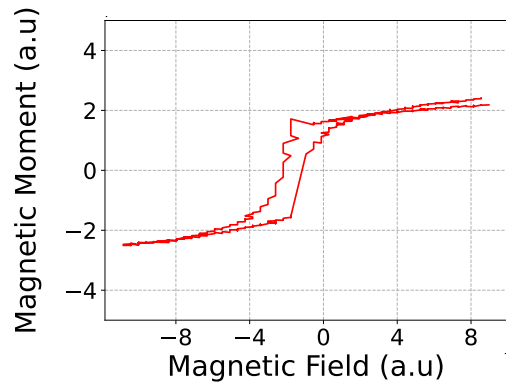influence of these parameters on the magnetic response of the samples.

Figure 4.5: MOKE analysis of a) sample 1 at 0°), b) sample 1 at 90°), sample 3, d) sample 5, and e) sample 6. Refer to Table 4.1 for sample details.
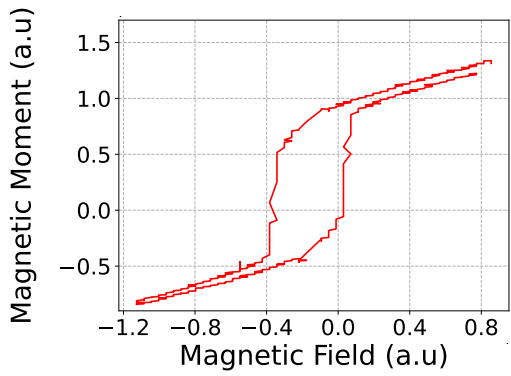
4.4 VSM Analysis of YIG films

Figure 4.6 compares the hysteresis loop obtained from the VSM analysis for the YIG films with varying thickness and annealing parameters.
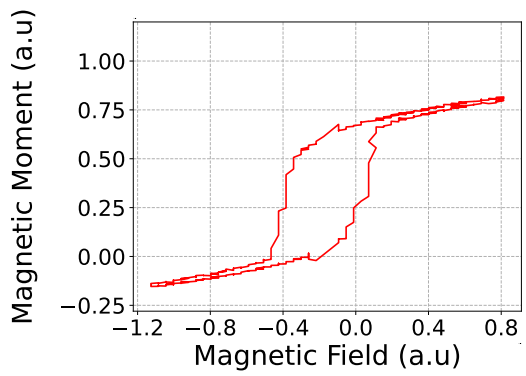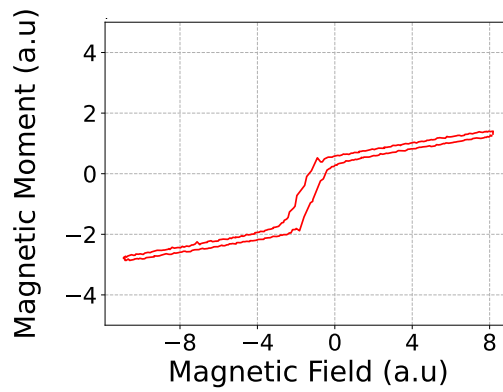
(a)

(b)

(c)

(d)

(e)

Figure 4.6: VSM analysis of a) sample 1 at 0°), b) sample 1 at 90°), sample 3, d) sample 5, and e) sample 6 (details in Table 4.1).

Chapter 5

Conclusion

5.1   Summary

This thesis explored the production of high-quality nanometer-scale YIG films via radio frequency (RF) magnetron sputtering, ensuring the reproducibility and maintenance of the properties of bulk YIG in these films. The research focused on analyzing the magnetic and structural characteristics of YIG, particularly in optimizing growth parameters and the heat treatment of the films. Regarding magnetic properties, the study examined how the dissipation term, specifically the Gilbert damping constant (α), is influenced by deposition conditions and heat treatment. By adjusting the thickness and annealing parameters, the static and dynamic magnetization of YIG thin films were investigated. The lowest observed Gilbert damping constant was 2.1 x 10^{-3}, achieved with a sample that had a deposition time of 31 minutes and was annealed at 900°C for 6 hours.

5.2   Perspectives for Future Work

1. **Optimization of Growth Conditions:** Future research endeavors will focus on further refining the growth conditions to achieve high-quality monocrystalline YIG films with the minimal damping constant.

2. **Temperature and Angle-Dependent Ferromagnetic Resonance (FMR) Analysis:** Future investigations will involve conducting comprehensive studies on temperature and angle-dependent FMR characteristics of these films. Such analyses will provide valuable insights into the temperature and orientation dependencies of their magnetic properties.

3. **Formation of YIG/Heavy Metals (HMs) Bilayers:** Exploring the formation of bilayers comprising YIG and Heavy Metals (HMs) will allow for the exploration of spin-to-charge current conversion phenomena. This research direction holds promise for advancing our understanding of spintronic devices.

4. **Exploration of YIG/2-D Transition Metal Dichalcogenides (TMDs) Bilayers:** Another avenue for future exploration involves creating bilayers composed of YIG and 2-D Transition Metal Dichalcogenides (TMDs). This will facilitate the investigation of spin and charge current dynamics within these hybrid systems, offering potential applications in spintronics and beyond.

5. **Investigation into the Inverse Spin Hall Effect (ISHE):** Further inquiry into the Inverse Spin Hall Effect (ISHE) will deepen our understanding of the interplay between spin currents and electrical currents in YIG-based systems. Such investigations are crucial for the development of novel spintronic devices and materials.

References

[1] A. Oliveira, R. Rodríguez-Suárez, M. Correa, F. Bohn, S. Raza, R. Sommer, and C. Chesman. Filtering magnetic relaxation mechanisms of yig (001) thin films using ferromagnetic resonance. *Journal of Magnetism and Magnetic Materials*, 507:166851, 2020.

[2] B. Dieny, I. L. Prejbeanu, K. Garello, P. Gambardella, P. Freitas, R. Lehndorff, W. Raberg, U. Ebels, S. O. Demokritov, J. Akerman, A. Deac, P. Pirro, C. Adelmann, A. Anane, A. V. Chumak, A. Hirohata, S. Mangin, S. O. Valenzuela, M. C. Onbaşlı, and M. d'Aquino. Opportunities and challenges for spintronics in the microelectronics industry. *Nature Electronics*, 3(8):446–459, 2020. DOI: https://doi.org/10.1038/s41928-020-0461-5. URL: https://doi.org/10.1038/s41928-020-0461-5.

[3] J. Ding, T. Liu, H. Chang, and M. Wu. Sputtering growth of low-damping yttrium-iron-garnet thin films. *IEEE Magnetics Letters*, 11:1–5, 2020.

[4] S. Satapathy, P. Siwach, H. Singh, R. Pant, and K. Maurya. Structural and magnetic properties of yig thin films deposited by pulsed laser deposition and rf magnetron sputtering technique. *Physica Scripta*, 98(10):105508, 2023.

[5] A. B. d. Oliveira, C. Chesman, R. Rodríguez-Suárez, R. Da Costa, U. Silva, N. Da Costa, B. Silva, R. L. Sommer, F. Bohn, and M. Correa. Effects of second order surface anisotropy in yig sputtered onto ggg (1 0 0) oriented substrate. *Journal of Magnetism and Magnetic Materials*, 469:64–68, 2019.

[6] A. Mitra. Structural and magnetic properties of yig thin films and interfacial origin of magnetisation suppression. 2017. URL: `https://etheses.whiterose.ac.uk/18696/1/Arpita%20Mitra_FinalThesis.pdf`. [Accessed 16 May 2024].

[7] S. Sailler, G. Skobjin, H. Schlörb, B. Boehm, O. Hellwig, A. Thomas, S. Goennenwein, and M. Lammel. Crystallization dynamics of amorphous yttrium iron garnet thin films. *arXiv preprint arXiv:2308.00412*, 2023.

[8] A. Z. Arsad, A. W. M. Zuhdi, N. B. Ibrahim, and M. A. Hannan. Recent advances in yttrium iron garnet films: methodologies, characterization, properties, applications, and bibliometric analysis for future research directions. *Applied Sciences*, 13(2):1218, 2023.

[9] R. Xiang, L. Chen, S. Zhang, H. Li, J. Du, Y. Du, and R. Liu. Electrical generation and detection of spin waves in polycrystalline yig/pt grown on silicon wafers. *Materials Research Express*, 7(4):046105, 2020.

[10] R. Torrão, O. Alves, B. Archanjo, L. Sampaio, and F. Garcia. Reproducible low gilbert damping yttrium iron garnet by magnetron sputtering. *Journal of Alloys and Compounds*, 923:166300, 2022.

[11] N. A. Spaldin. *Magnetic Materials: Fundamentals and Applications*. Cambridge University Press, 2010.

[12] M. Basit. Ferromagnetic resonance for investigating magnetization dynamics in magnetic thin films. 2021. URL: `https://physlab.org/wp-content/uploads/2021/05/Basit_FMR_Thesis-min.pdf`. [Accessed 16 May 2024].

[13] GitHub. Fmr-data-filtration-and-visualization/tutorial.ipynb at main · mahadnav/fmr-data-filtration-and-visualization. n.d. URL: `https://github.com/mahadnav/FMR-Data-Filtration-and-Visualization/blob/main/Tutorial.ipynb`. [Accessed 16 May 2024].

[14]   mahadnav. Vna-fmr-model-fitting-and-analysis/vna model fitting.ipynb at
         main · mahadnav/vna-fmr-model-fitting-and-analysis. 2024. URL: `https:`
         `//github.com/mahadnav/VNA-FMR-Model-Fitting-and-Analysis/blob/`
         `main/VNA%20Model%20Fitting.ipynb`. [Accessed 3 Jul. 2024].